8630–8640 *Nucleic Acids Research, 2018, Vol. 46, No. 16* *Published online 18 July 2018*
doi: 10.1093/nar/gky642

Crystal structure of dimeric human PNPase reveals why disease-linked mutants suffer from low RNA import and degradation activities

Bagher Golzarroshan[1,2,3], Chia-Liang Lin[1], Chia-Lung Li[1], Wei-Zen Yang[1], Lee-Ya Chu[1,2,3], Sashank Agrawal[1,4,5] and Hanna S. Yuan[1,2,4,*]

[1]Institute of Molecular Biology, Academia Sinica, Taipei, Taiwan 11529, Republic of China, [2]Chemical Biology and Molecular Biophysics Program, Taiwan International Graduate Program, Academia Sinica, Taipei, Taiwan 11529, Republic of China, [3]Institute of Bioinformatics and Structural Biology, National Tsing Hua University, Hsinchu, Taiwan 30013, Republic of China, [4]Molecular and Cell Biology Program, Taiwan International Graduate Program, Academia Sinica, Taipei, Taiwan 11529, Republic of China and [5]Graduate Institute of Life Sciences, National Defense Medical Center, Taipei, Taiwan 11490, Republic of China

Received May 04, 2018; Revised June 13, 2018; Editorial Decision July 04, 2018; Accepted July 16, 2018

ABSTRACT

Human polynucleotide phosphorylase (PNPase) is an evolutionarily conserved 3′-to-5′ exoribonuclease principally located in mitochondria where it is responsible for RNA turnover and import. Mutations in PNPase impair structured RNA transport into mitochondria, resulting in mitochondrial dysfunction and disease. PNPase is a trimeric protein with a doughnut-shaped structure hosting a central channel for single-stranded RNA binding and degradation. Here, we show that the disease-linked human PNPase mutants, Q387R and E475G, form dimers, not trimers, and have significantly lower RNA binding and degradation activities compared to wild-type trimeric PNPase. Moreover, S1 domain-truncated PNPase binds single-stranded RNA but not the stem–loop signature motif of imported structured RNA, suggesting that the S1 domain is responsible for binding structured RNAs. We further determined the crystal structure of dimeric PNPase at a resolution of 2.8 Å and, combined with small-angle X-ray scattering, show that the RNA-binding K homology and S1 domains are relatively inaccessible in the dimeric assembly. Taken together, these results show that mutations at the interface of the trimeric PNPase tend to produce a dimeric protein with destructive RNA-binding surfaces, thus impairing both of its RNA import and degradation activities and leading to mitochondria disorders.

INTRODUCTION

Import of selected macromolecules into mitochondria, including proteins and RNAs encoded by the nuclear genome, is essential for mitochondrial biogenesis (1,2). In contrast to the protein import machinery, import pathways of RNAs into mitochondria are less clear, even though imported RNAs are essential for mitochondrial DNA replication and protein translation (3). Diverse mechanisms have been proposed for RNA import into mitochondria, including the involvement of polynucleotide phosphorylase (PNPase) in importing small structured RNAs with a signature stem–loop motif (4,5). Consistent with the importance of this process, mutations in human PNPase are linked to various mitochondrial diseases characterized by respiratory-chain deficiency and oxidative phosphorylation defects (6–10).

PNPase is an evolutionary conserved 3′-to-5′ exoribonuclease that degrades RNA from the 3′ end by a phosphorolysis mechanism (11–14). The gene encoding for human PNPase, *PNPT1*, was first identified as an up-regulated gene during cellular senescence and terminal differentiation (15). Upon expression induced by type I interferons, PNPase degrades *c-myc* mRNA in cytoplasm, as well as a subset of microRNAs, and the enzyme is thought to be involved in a wide range of cellular and pathological processes including differentiation, proliferation, tumorigenesis and aging (16–18). Human PNPase possesses a mitochondrial localization sequence (MLS) at its N-terminus, so it is trafficked to mito-

*To whom correspondence should be addressed. Tel: +886 2 2788 4151; Fax: +886 2 2782 6085; Email: hanna@sinica.edu.tw

chondria where it is primarily located in the intermembrane space (19,20). There, it is associated with importing structured RNA into the mitochondrial matrix, including RNase P RNA, MRP RNA, 5S rRNA and microRNAs (4,5,18). A small amount of PNPase is also localized within the mitochondrial matrix where it degrades mitochondrial RNA in cooperation with Suv3 helicase (21).

PNPase from different species shares a similar domain structure, consisting of two RNase PH domains (PHI and PHII), single α-helical, K homology (KH) and S1 domains (Figure 1A) (22). Previously reported crystal structures of bacterial and human PNPase show a conserved trimeric doughnut-shaped architecture, with a central channel formed by the six RNase PH domains through which the 3′ end of a single-stranded RNA (ssRNA) molecule is threaded to interact with the catalytic site in one of the PHII domains (one of the catalytic residues, Ser484, is labeled in Figure 1B) (23–27). The S1 and KH domains are involved in RNA binding, so mutations or deletions of either of these domains disrupt RNA binding to varying extents (23,24,28). KH domains play an important role in RNA binding in many proteins (29). The conserved GXXG loops of the three KH domains in human PNPase are oriented inward to form a KH pore that plays the principal role in ssRNA interactions (23).

Homozygous mutations in human PNPase, including Q387R and E475G, were first characterized in patients exhibiting mitochondrial dysfunctions and diseases, including hearing loss and respiratory-chain deficiency (6,7). PNPase in these patients is expressed but does not assemble into trimeric proteins likely because the mutations disrupt hydrogen-bonding networks in the trimeric interfaces (Figure 1B). Consequently, these mutants fail to import structured RNA into mitochondria (6,7). Disease-linked heterozygous variants have also been identified, including Q254K/A510P that causes severe multisystem disease (8), R136H/P140L that linked to Leigh syndrome (9) and G76D/R192* (* indicating nonsense mutation) that causes delayed myelination (10). It has been shown that the mutations of R136H/P140L produced RNA degradation-inactive PNPase enzyme (9), and Q254K/A510P resulted in a lower level of PNPase that cannot assemble into a trimeric complex (8). However, the molecular bases for why these mutants lost the ability to assemble into a functional timer are not clear.

Here, we expressed and purified two human PNPase mutants, Q387R and E475G, and show that they are uncharacteristically folded as dimers and exhibit low ssRNA binding and degrading activities. We further determined the crystal structure and conducted small-angle X-ray scattering (SAXS) analysis on the dimeric form of PNPase and reveal that its KH and S1 domains are mostly inaccessible in the dimeric assembly. We also show that S1 domains in trimeric PNPase form an S1 pore that is likely involved in binding to the stem–loop signature motif of imported structured RNA. We conclude that mutations disrupting the PNPase trimeric conformation tend to produce dimeric proteins that present impaired RNA binding and degradation activities, thus leading to mitochondrial dysfunction and diseases.

MATERIALS AND METHODS

Cloning, protein expression and purification

The cDNA encoding the full-length human PNPase without its MLS (residues 46–783) and the S1 domain-truncated mutant PNPase-ΔS1 (residues 46–669) were amplified by polymerase chain reaction using Taq DNA polymerase (Stratagene) and subcloned into NcoI/NotI sites of the expression vector pET28b (Novagen) to generate the C-terminal His-tagged constructs or into NheI/SalI sites of the expression vector pET28a (Novagen) to generate the N-terminal His-tagged constructs. The plasmids encoding PNPase mutants, Q387R, E475G and S484A, were generated by the QuickChange site-directed mutagenesis kit (Stratagene) from the pET28b construct containing the wild-type PNPase cDNA for the expression of the C-terminal His-tagged PNPase mutants. All constructs, including the ones encoding PNPase, PNPase-S484A, PNPase-ΔS1, PNPase-ΔS1-S484A, PNPase-Q387R, PNPase-Q387R-S484A, PNPase-E475G and PNPase-E475G-S484A, were transformed into the *Escherichia coli* strain BL21-CodonPlus (DE3)-RIPL (Stratagene) and incubated at 37°C overnight in LB medium supplemented with 50 μg/ml kanamycin. The cultures were grown to an OD_{600} of 0.6 and then induced with 0.5 mM IPTG at 18°C for 20 h. The harvested cells were disrupted by a microfluidizer (Microfluidics M-110P) in buffers containing 50 mM Tris (pH 7.4), 1 M NaCl and 10 mM imidazole. Crude cell extracts were passed through a His-Trap HP column (GE HealthCare), and PNPase proteins were eluted with a gradient of 0–500 mM imidazole in 50 mM Tris–HCl, pH 7.4 and 500 mM NaCl. Eluted protein fractions were combined and diluted with a buffer containing 50 mM Tris–HCl, pH 7.4 and 10 mM ethylenediaminetetraacetic acid (EDTA). The protein sample was then passed through a HiTrap heparin column (GE Healthcare) and eluted with a gradient of 0–1 M NaCl in a buffer of 50 mM Tris–HCl, pH 7.4 and 10 mM EDTA. To separate trimeric and dimeric forms of PNPase-NHis, protein fractions eluted from HiTrap heparin column were diluted with 25 mM HEPES (pH 7.0) and 1 M $(NH_4)_2SO_4$ and loaded into a Phenyl HP Column (HiTrap™, GE Healthcare) and eluted with a gradient of 1–0 M $(NH_4)_2SO_4$ in the buffer of 25 mM HEPES (pH 7.0) (Supplementary Figure S1). The purified PNPase sample was further applied to a gel filtration column (Superdex 200 Increase 10/300 GL, GE Healthcare) and eluted with a buffer of 20 mM HEPES (pH 7.4) and 300 mM KCl. Purified protein samples were concentrated to suitable concentrations and stored at −80°C until use.

Multiangle light scattering (MALS)

Protein samples of PNPase-CHis, PNPase-NHis, PNPase-Q387R and PNPase-E475G (100 μl injection volumes) were applied to Agilent Bio SEC-3 columns (Agilent Technologies) connected to a DAWN HELIOS II-18 angle MALS (Wyatt Technology) detector with wavelength set at 658 nm. Samples equilibrated in 20 mM HEPES (pH 7.4) and 300 mM KCl were run at a flow rate of 0.2 ml/min using the ÄKTA-UPC 900 FPLC system (GE Healthcare). ASTRA

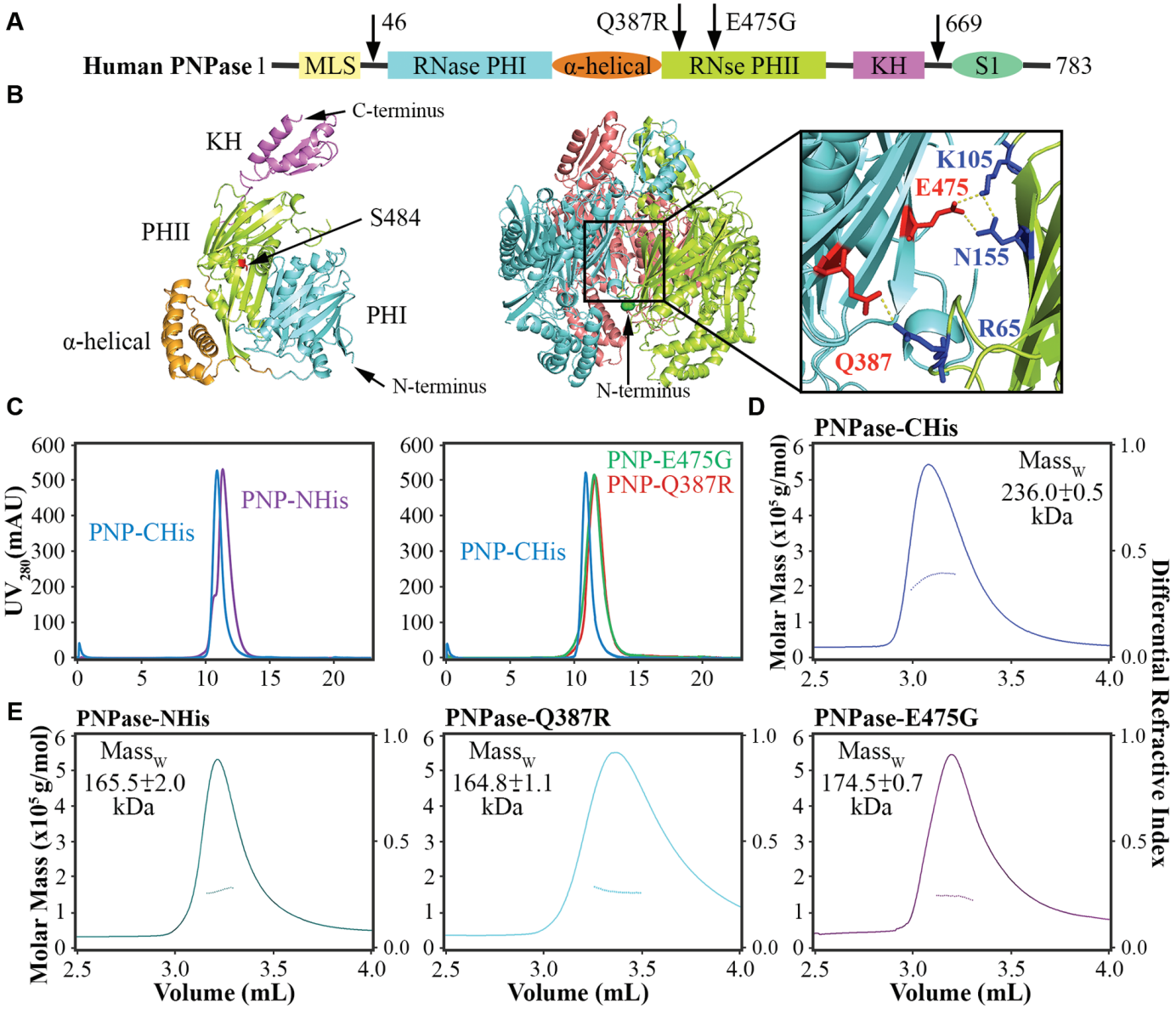

Figure 1. Disease-linked human PNPase mutants are assembled into dimers, not trimers. (**A**) The domain organization of human PNPase. The disease-linked mutations, Q387R and E475G, are located in the RNase PHII domain. (**B**) Disease-linked mutations are located at the trimeric interface in the crystal structure of PNPase-ΔS1 (PDB ID: 3U1K). (**C**) Gel filtration profiles reveal that PNPase-CHis elutes in a single peak as a trimer, whereas PNPase-NHis elutes in two peaks. Disease-linked PNPase-Q387R and PNPase-E475G, both with a C-terminal His-tag, elute in a single peak with a smaller oligomeric form compared to PNPase-CHis. (**D** and **E**) Molecular weights of PNPase-CHis, PNPase-NHis, PNPase-Q387R and PNPase-E475G were estimated by SEC-MALS and are represented as elution profiles.

software (Wyatt Technology) was used to analyze ultraviolet fluorescence, MALS, and refractive index data.

Differential scanning fluorimetry (DSF)

Differential scanning fluorimetry (DSF) was performed by the LightCycler® 480 instrument (Roche) with the excitation wavelength of 483 nm and emission wavelength of 568 nm, using the protocols described previously (30). A total of 20 μl sample containing 100 ng of PNPase in a buffer of 50 mM Tris–HCl, pH 7.4, 300 mM KCl and 5X SYPRO Orange (Invitrogen) dye was loaded on a multiwell plate (MultiWell Plate 96 White (Roche)) in triplicate and sealed with LightCycler® 480 Sealing Foil (Roche). Reactions were incubated for 10 min at room temperature before starting the thermal melting analysis. The temperature was increased from 20 to 80°C at a heating rate of 0.012°C/s, and the fluorescence intensity was measured at intervals of 0.02°C (Supplementary Figure S2). The melting temperature (T_m) values were determined by the LightCycler® Protein Melting Analysis.

RNase activity assays

For the RNA degradation experiments, PNPase proteins (10 nM)—including PNPase-CHis, PNPase-NHis, PNPase-

Q387R and PNPase-E475G—were incubated with a 37-nt fluorescein-labeled ssRNA with a sequence of 5′-FAM-C_7U_{30}-3′ (10 nM, purchased from Dharmacon) at 37°C for 0–60 min in a reaction buffer containing 20 mM Tris–HCl (pH 7.5), 100 mM NaCl, 1 mM DTT, 2 mM NaH_2PO_4 and 0.25 mM $MgCl_2$. The RNA degradation reactions were stopped by adding 2× urea loading dye (Thermo) at different time-points (0, 15, 30, 45 and 60 min) and heating at 90°C for 3 min. Samples were then loaded on a 20% TBE–urea polyacrylamide denaturing gel for electrophoresis, which was scanned with a Typhoon FLA 9000 system (GE Healthcare).

RNA binding by fluorescence polarization assays

RNA-binding affinities for PNPase-S484A, PNPase-Q387R-S484A, PNPase-E475G-S484A and PNPase-ΔS1-S484A with single-stranded and stem–loop RNAs were determined by measuring the changes in fluorescence polarization using a Paradigm plate reader (Molecular Devices). The 5′-end fluorescein-labeled ssRNA with a sequence of 5′-FAM-UUUUUUUUUUUUUUU-3′ and the stem–loop RNA with a sequence of 5′-FAM-UCGCAGCGUAUCCCGCUGCGC-3′ at a final concentration of 2 nM were titrated with the indicated concentrations of PNPase in a binding buffer of 20 mM Tris–HCl (pH 7.4), 50 mM KCl, 100 μg/ml bovine serum albumin, 0.1 mM EDTA, 1 mM DTT, 10% glycerol and 2 mM $MgCl_2$. Reactions were incubated at 37°C for 30 min and then read at 538 nm at an excitation of 485 nm. Equation (1) was used to calculate fluorescence polarization (FP), where I_{para} and I_{perp} represent the fluorescence intensities of signals in the parallel and perpendicular planes, respectively. The calculated FP values were plotted against PNPase concentration and the curves were fitted through equation (2) to obtain the K_d value.

$$\mathrm{mFP} = 1000 * \left(\frac{I\mathrm{para} - I\mathrm{perp}}{I\mathrm{para} + I\mathrm{perp}} \right) \quad (1)$$

$$y = \mathrm{FPmin} + \left[\frac{\mathrm{FPMax} - \mathrm{FPMin}}{1 + \left(\frac{x}{Kd} \right)^n} \right] \quad (2)$$

Crystallization and crystal structure determination

Dimeric PNPase-ΔS1-NHis was crystallized by the hanging-drop vapor diffusion method by mixing 1 μl of protein sample (10 mg/ml in 50 mM Tris–HCl, pH 7.4 and 150 mM NaCl) and 1 μl of reservoir solution (0.1 M citrate buffer, pH 5.0, 10% (v/v) 2-propanol and 26% (v/v) polyethylene glycol 400). X-ray diffraction data were collected at beamline BL44XU at SPring-8, Harima, Japan and processed by HKL2000 software. The structure was solved by the molecular replacement method using the crystal structure of one protomer of the trimeric form of human PNPase-ΔS1 (PDB ID: 3U1K) as the search model in the program MOLREP of CCP4. The structure model was built using Coot and refined in Phenix.

Small-angle X-ray scattering (SAXS)

SAXS data were recorded at the SAXS beamline 23A coupled to a high-performance liquid chromatography system that was connected to the Agilent-Bio SEC-3 300 Å column in the National Synchrotron Radiation Research Center in Hsinchu, Taiwan. A protein sample (5 mg/ml for PNPase-CHis, PNPase-NHis, PNPase-Q387R or PNPase-E475G in 20 mM HEPES, pH 7.4, 300 mM KCl) of 100 ml was injected into the Agilent-Bio SEC-3 column (300 Å pore size) at a flow rate of 0.02 ml/min and detected at a sample-to-detector distance of 2.3 m. An X-ray wavelength of 0.8266 Å was used to collect 34 frames of 30-s exposure for all samples. Selected frames were merged and analyzed for initial R_g estimation by the PRIMUS program, D_{max} and $P(r)$ distance distribution by the GNOM program. The calculate SAXS profiles from the crystal structure were generated by CYSOL (ATSAS program suite, version 2.7). Ensemble optimization method (EOM) analysis was performed using the web interface of EMBL Hamburg (31). The crystal structure of trimeric PNPase-ΔS1 (PDB ID: 3U1K) or dimeric PNPase-ΔS1 (this study, PDB ID: 5ZF6) and the homology-modeled S1 domain (by SWISS-MODEL web server based on the crystal structure of the S1 domain in *Coxiella burnetii* PNPase, PDB ID: 4NBQ) (32) were used as rigid bodies in the ensemble search. A total of 10 000 models were first generated, and then the SAXS profiles of these models were fitted with the measured SAXS profiles to select the best-fitting models. Two subset conformers of PNPase, open and close were selected, and their ensemble gave comparable fitting curves to the experimental SAXS data (Figure 4C and D).

RESULTS

Disease-linked PNPase mutants are primarily dimeric proteins

To understand the molecular basis for loss-of-function of disease-linked PNPase mutants, we expressed and purified two wild-type PNPase proteins lacking the N-terminal MLS—referred to, respectively, as PNPase-CHis (residues 46–783) hosting a C-terminal His-tag, and PNPase-NHis (residues 46–783) hosting an N-terminal His-tag—as well as two PNPase mutants (PNPase-Q387R and PNPase-E475G), with both of these latter harboring a C-terminal His-tag. All recombinant proteins were purified to a high homogeneity by chromatographic methods. The wild-type PNPase-CHis eluted in a single peak in size exclusion chromatography (SEC) and with an elution volume that suggested a trimeric conformation (Figure 1C). PNPase-NHis eluted in a major peak with a shoulder; the major peak corresponded to a smaller oligomeric form, likely a dimer or monomer, whereas the shoulder matched the trimeric form (Figure 1C). We noticed that the N-terminal end of PNPase was located closely to the trimeric interface and therefore the N-terminal His-tag likely interfered with protein trimerizaton (Figure 1B). This result suggests that PNPase-CHis with a C-terminal His-tag is a stable trimer, but that the N-terminal His-tag of PNPase-NHis destabilizes the trimeric conformation and consequently tends to assemble into a mixture of trimer and dimer/monomer.

In contrast, the two disease-linked mutants, PNPase-Q387R and PNPase-E475G (both with a C-terminal His-tag), eluted in one peak with an elution volume similar to that of the smaller oligomeric form of PNPase-NHis (Figure 1C). To verify these oligomeric forms, we conducted size exclusion chromatography-coupled multiangle light scattering (SEC-MALS) and found that PNPase-CHis is a trimer with a molecular weight of 236.0 kDa (calculated MW for a trimer: 246.9 kDa) (Figure 1D), whereas the two mutated proteins assemble into dimers with a MW of 164.8 kDa for PNPase-Q387R and 174.5 kDa for PNPase-E475G (calculated MW for a dimer: 164.6 kD) (Figure 1E). We further isolated the major peak of the dimeric fractions of PNPase-NHis from gel filtration and measured a MW of 165.5 kDa by SEC-MALS, confirming that PNPase-NHis primarily formed dimers (see Figure 1E). To test the thermal stability of trimeric and dimeric forms of PNPase, we measured the thermal melting points of PNPase proteins by DSF (Supplementary Figure S2). The trimeric PNPase-CHis and dimeric PNPase-NHis had similar melting points of 54 and 55°C, respectively, whereas the two disease-linked mutants, PNPase-Q387R and PNPase-E457G, had melting points of 53–54°C. These results suggest that trimeric and dimeric forms of PNPase have comparable thermal stability. Taken together, these results show that the wild-type PNPase with a C-terminal His-tag is properly folded as a trimeric enzyme, whereas the two disease-linked mutants (PNPase-Q387R and PNPase-E475G) are folded into dimers.

Dimeric PNPase exhibits impaired RNA binding and degradation activities

To test the RNA-binding and degrading activities of the disease-linked mutants, we incubated PNPase proteins with 5′-end fluorescein-labeled 37-nt ssRNA (5′-FAM-C_7U_{30}-3′) in the degradation buffer at 37°C. The wild-type trimeric PNPase-CHis rapidly degraded ssRNA into the final products of about four nucleotides (23) in our time-course experiments, whereas the dimeric PNPase-NHis poorly degraded ssRNA as most of the 37-nt substrates were not degraded (Figure 2A). The two disease-linked mutants, PNPase-Q387R and PNPase-E475G, also exhibited limited RNA degradation ability relative to wild-type trimeric PNPase, with most of the 37-nt ssRNA substrates remaining intact in the gel.

We further measured the RNA-binding activity of the disease-linked PNPase mutants using 5′-end fluorescein-labeled 15-nt ssRNA (5′-FAM-U_{15}-3′) by fluorescence polarization. To avoid RNA degradation by PNPase, all proteins were inactivated by mutating the catalytic Mg^{2+}-binding residue Ser484 to alanine to produce trimeric PNPase-S484A and dimeric PNPase-Q387R-S484A and PNPase-E475G-S484A (conformations confirmed by SEC, data not shown). Trimeric PNPase-S484A bound ssRNA (5′-FAM-U_{15}-3′) with a high affinity (K_d = 0.028 μM, Figure 2B), whereas the two dimeric mutants bound ssRNA with much lower affinities (K_d = 7.6 μM for PNPase-Q387R-S484A and K_d = 8.0 μM for PNPase-E475G-S484A, Figure 2D). This result shows that these disease-linked dimeric PNPase mutants have significantly limited ssRNA-binding activities.

Transport of structured RNA with a signature stem–loop motif into mitochondria is impaired in the disease-linked PNPase mutants (5). To determine if the disease-linked PNPase mutants can bind stem–loop RNA, we further measured by fluorescence polarization the binding affinities of PNPase proteins to the stem–loop motif of MRP RNA. Trimeric PNPase-S484A bound the stem–loop RNA with a high affinity (K_d = 0.21 μM, Figure 2B). In contrast, neither of the two disease-linked mutants (PNPase-Q387R-S484A and PNPase-E475G-S484A) could bind the stem–loop RNA since we could not detect a significant fluorescence signal (data not shown). These results indicate that the disease-linked PNPase proteins are impaired in terms of mitochondrial RNA import because they cannot interact with the signature stem–loop motif of imported structured RNAs.

The S1 domain of PNPase is responsible for interacting with stem–loop RNA

To determine which domain of PNPase is involved in binding to the stem–loop RNA, we expressed and purified an inactive S1 domain-truncated PNPase mutant with a C-terminal His-tag, referred to as PNPase-ΔS1-S484A, for RNA-binding assays. PNPase-ΔS1-S484A eluted as a trimeric enzyme (data not shown), consistent with previous data showing that the S1 domain is not required for protein trimerization (23). We found that PNPase-ΔS1-S484A bound ssRNA (5′-FAM-U_{15}-3′) with a high affinity (K_d = 0.030 μM), i.e. similar to full-length PNPase-S484A, suggesting that the S1 domain is not responsible for ssRNA binding (Figure 2C). This outcome is consistent with an earlier report showing that the KH domain, but not the S1 domain, in human PNPase is involved in binding to ssRNA (23). However, similar to the disease-linked PNPase mutants, PNPase-ΔS1-S484A failed to interact with the stem–loop RNA (no significant fluorescence signal detected, summarized in Figure 2D). Taken together, these results suggest that the S1 domain of PNPase is involved in binding to the stem–loop motif of imported structured RNA for mitochondrial RNA import.

Crystal structure of dimeric PNPase-ΔS1 reveals a disrupted KH pore

To investigate the molecular basis for the loss-of-function of the disease-linked PNPase mutants, we further screened the crystallization conditions for the dimeric forms of the PNPase mutants, but none yielded diffractable crystals. We then further purified the dimeric form of PNPase using the N-terminal-His-tagged proteins, including PNPase-NHis and PNPase-ΔS1-NHis. These latter two proteins formed a mixture of trimers and dimers that could be further separated by reverse phase chromatography (see Supplementary Figure S1). Only dimeric PNPase-ΔS1-NHis yielded crystals that diffracted X-rays to a resolution of 2.8 Å. We solved the structure of dimeric PNPase-ΔS1-NHis by molecular replacement using the crystal structure of a single protomer from trimeric PNPase-ΔS1 (PDB ID: 3U1K) as the search model. We found that two molecules formed a dimeric structure in one asymmetric unit in the $P2_1$ mono-

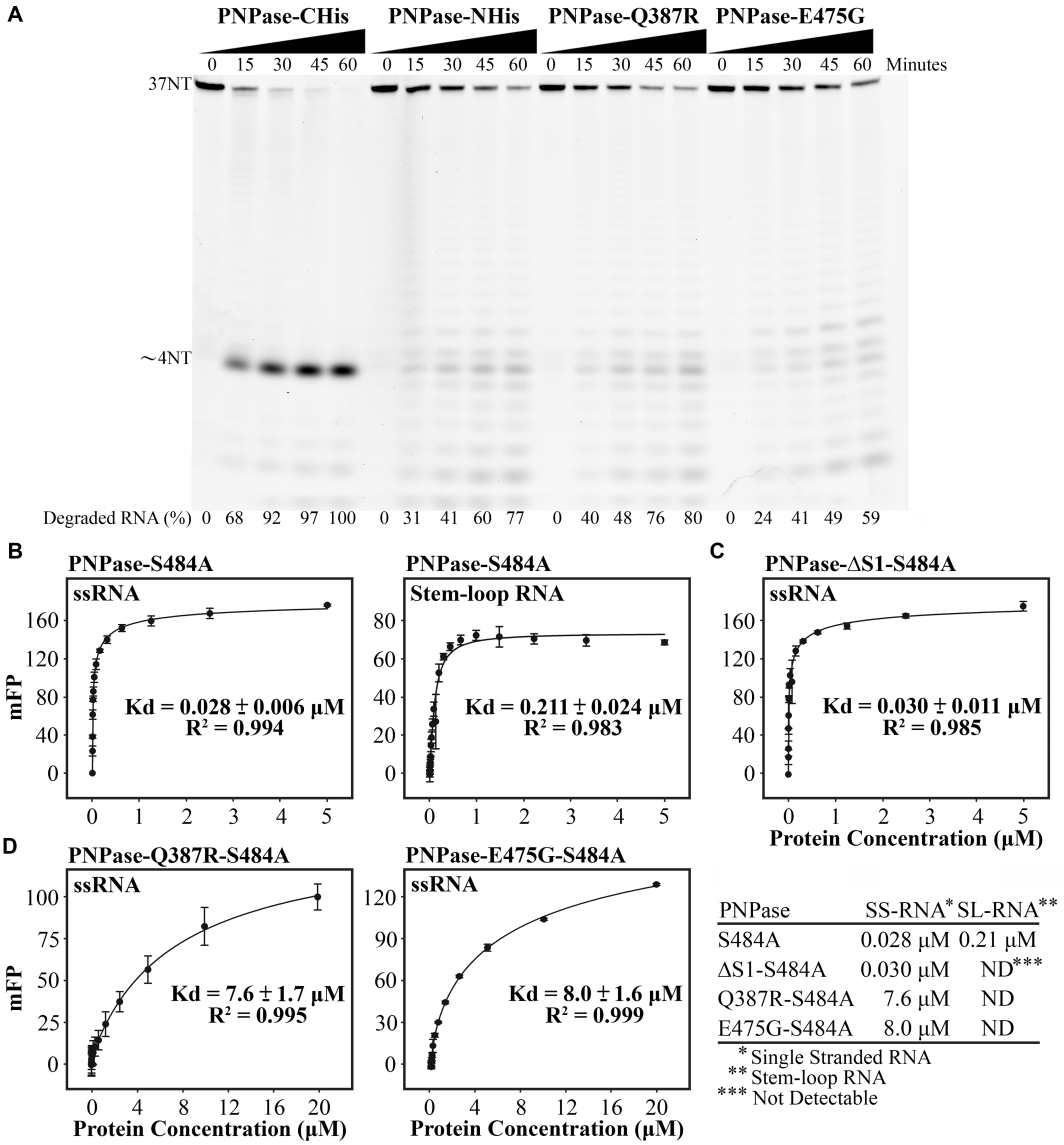

Figure 2. Disease-linked PNPase mutants exhibit impaired RNA binding and degradation activities. (**A**) Trimeric PNPase-CHis (10 nM) degraded 37-nt ssRNA (10 nM) with a sequence of 5′-FAM-C_7U_{30}-3′ more efficiently than dimeric forms of the enzyme, including PNPase-NHis, PNPase-Q387R and PNPase-E475G. The percentages of substrate (37-nt ssRNA) that were degraded by PNPase in the time-course experiments were listed at the bottom of the gel (with 0 min setting to 0%). (**B**–**D**) RNA-binding affinities of PNPase proteins were measured by fluorescence polarization (in mFP units) and are plotted against protein concentrations. The RNA substrates used are stated in the respective graph, with 'ssRNA' representing 5′-FAM-UUUUUUU UUUUUUUU-3′ and 'Stem–loop RNA' representing 5′-FAM-UCGCAGCGUAUCCCGCUGCGC-3′, both of which were labeled at the 5′ end with 6-carboxyfluorescein (FAM).

clinic unit cell. X-ray data collection and refinement statistics for dimeric PNPase-ΔS1-NHis are provided in Table 1.

Each protomer of the dimeric PNPase-ΔS1-NHis structure contains two visible RNase PH domains (PHI and PHII) linked by an α-helical domain, as well as a C-terminal KH domain (Figure 3B). Superimposition of the RNase PH and α-helical domains in dimeric PNPase-ΔS1-NHis (chain A, PDB ID: 5ZF6) with those of trimeric PNPase-ΔS1 (chain A, PDB ID: 3U1K) gave an average RMSD of 1.33 Å for the fitted domains (480 Cα atoms), and a slightly higher RMSD of 2.50 Å (64 Cα atoms) for KH domains, showing that each protomer retained their overall structure in dimeric and trimeric structure. The three KH domains in trimeric PNPase interact to form a KH pore, with their GXXG motifs facing inward toward the pore for RNA binding (Figure 3A). In contrast, the KH domains in dimeric PNPase do not interact with each other, instead interacting with the PHII domain of the other protomer (see trimer-to-dimer conformational change in Supplementary Movie S1). All the catalytic residues responsible for the phosphorylase activity of PNPase, including Arg446, Ser484, Asp538 and Asp544 (23), are exposed in the dimeric structure, explaining why the dimeric form of PNPase has residual ssRNA-degrading activity. However, the GXXG motifs in the KH domains of dimeric PNPase are far from each other, so they cannot interact for ssRNA

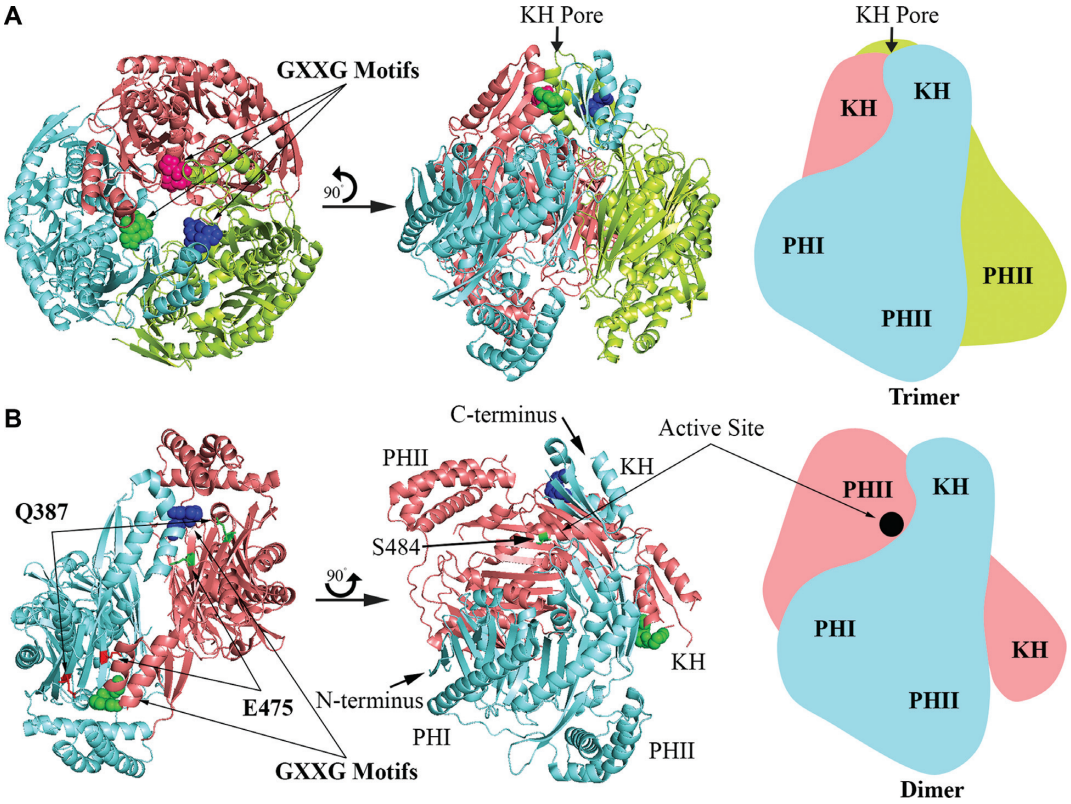

Figure 3. Comparison of the crystal structures of the dimeric and trimeric forms of S1-truncated human PNPase. (**A**) Crystal structure of the trimeric form of PNPase-ΔS1 (PDB ID: 3U1K). The GXXG motifs (in spheres) in the KH pore face inward toward the pore for ssRNA interactions. (**B**) Crystal structure of the dimeric form of PNPase-ΔS1-NHis (this study, PDB ID: 5ZF6). The KH pore is disrupted and the GXXG motifs are located far apart and mostly buried within the dimeric form. The active site residue S484 and the disease-linked mutational sites, Q387 and E475, are marked in the dimeric structure.

Table 1. X-ray diffraction and refinement statistics for dimeric PNPase-ΔS1-NHis

Data collection statistics	
Space group	$P2_1$
Cell dimensions, *a*, *b*, *c* (Å)	81.34 109.33 84.50
α, *β*, *γ* (°)	90.00 117.41 90.00
Wavelength (Å)	1.0
Resolution	50-2.80 (2.85-2.80)[a]
Observed reflections	106 714
Unique reflections	32 471
Data redundancy	3.3 (3.3)
Completeness	99.9 (99.8)
Rsym (%)	8.1 (57.0)
I/σ (I)	15.0 (2.3)
Refinement statistics	
Resolution range	42.2–2.8
Reflections (work/test)	28 918/1 930
R-work/R-free (%)	18.79/24.64
Number of atoms (Protein/Water)	8 555/66
Average B factor (Å^2)	36.0
RMSD in bound length (Å)	0.003
bond angle (°)	0.54
Ramachandran favored (%)	96.95
Ramachandran allowed regions (%)	3.05
Ramachandran outliers (%)	0

[a]Statistics for the highest resolution shell are shown in parentheses.

binding. Consequently, the dimeric form of PNPase exhibits reduced ssRNA binding and degradation activities relative to the trimeric form of PNPase. We conclude that the disrupted KH pore of the disease-linked dimeric PNPase mutants is responsible for impaired ssRNA-linked activities.

SAXS reveals that the S1 pore is also disrupted in dimeric PNPase

To determine the assembly of the S1 domain that was absent from our crystal structure study, we measured SAXS of the trimeric and dimeric forms of full-length PNPase. Trimeric PNPase-CHis had a distance distribution profile (Patterson function, $P(r)$) that was significantly different from those of dimeric PNPase proteins, including dimeric PNPase-NHis, PNPase-Q387R and PNPase-E475G (Figure 4A). PNPase-CHis exhibited D_{max} and R_g values of 165 and 44 Å, respectively, i.e. in agreement with those of a trimeric conformation. In contrast, all dimeric forms of PNPase exhibited lower D_{max} and R_g values (122–127 and 37–38 Å, respectively), consistent with the size of the crystal structure of dimeric PNPase-ΔS1-NHis.

Moreover, the SAXS profile for the S1 domain-truncated PNPase, PNPase-ΔS1-NHis, was also similar to those of the disease-linked mutants, PNPase-ΔS1-Q387R and PNPase-ΔS1-E475G (Supplementary Figure S3). These S1 domain-truncated dimeric PNPase all had a similar D_{max} of 99 Å and a R_g of 32–33 Å, indicating that all these dimeric PNPase proteins shared similar overall structures.

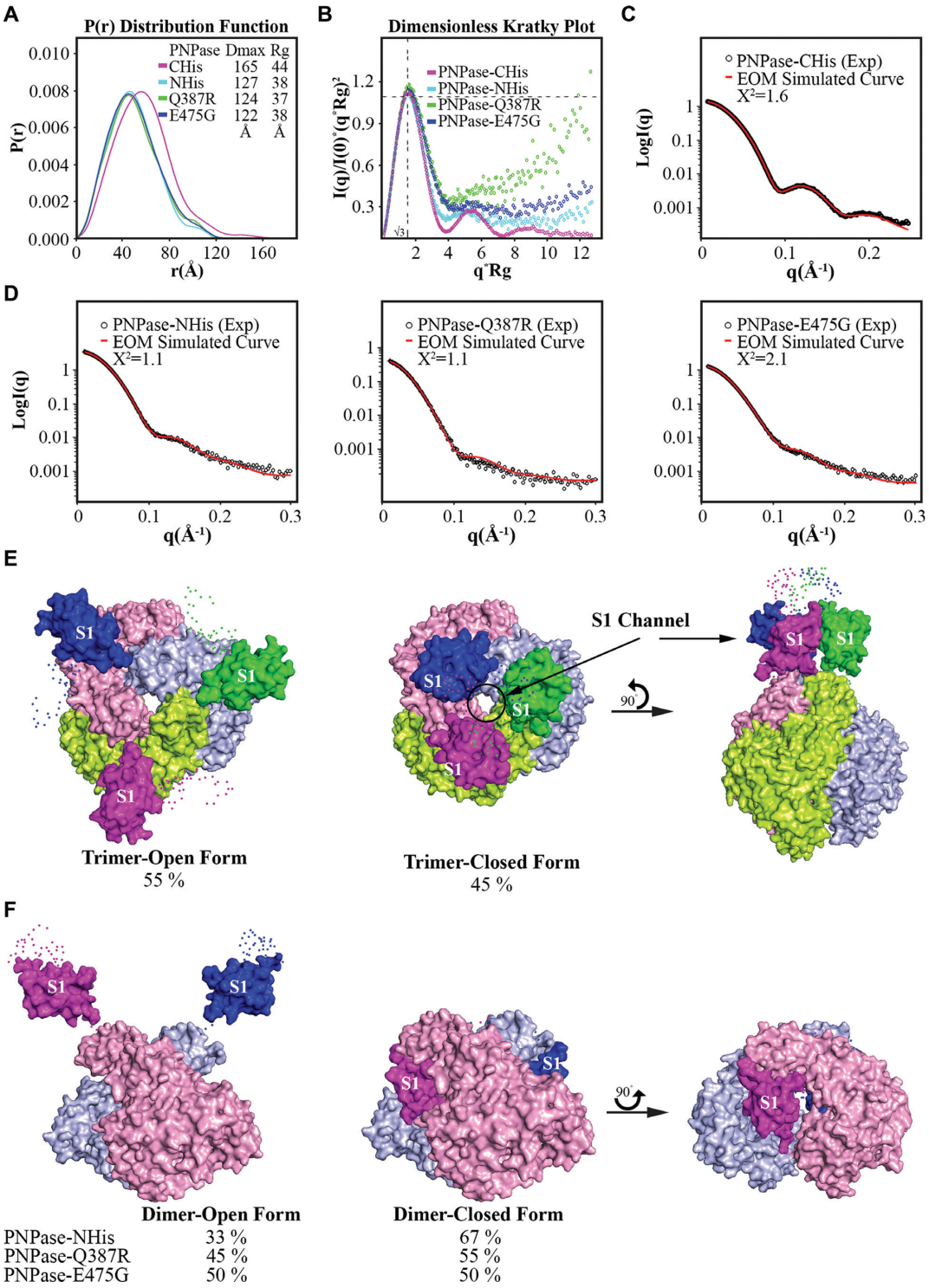

Figure 4. SAXS data analysis for trimeric and dimeric PNPase revealing a flexible S1 domain. (**A**) The $P(r)$ curves for three dimeric PNPase proteins are similar but different from that of trimeric PNPase-CHis. (**B**) The R_g-based dimensionless Kratky plot with curve peaks at $q^*R_g > \sqrt{3}$, indicating flexible conformations. (**C** and **D**) PNPase SAXS data were analyzed by the EOM. The experimental SAXS data fitted well with the calculated data from the EOM models (X^2 value indicated in the graphs). (**E**) Trimeric PNPase-CHis has two major ensemble conformations, open and closed, as generated by EOM. The three protomers are displayed in different colors. (**F**) Dimeric PNPase, including PNPase-NHis, PNPase-Q387R and PNPase-E475G, have two major conformations, open and closed, as generated by EOM.

Moreover, the calculated SAXS profile based on the crystal structure of PNPase-ΔS1-NHis was fitted well with the measured ones of PNPase-ΔS1-Q387R and PNPase-ΔS1-E475G. These results suggest that the disease-linked S1 domain-truncated PNPase mutants, PNPase-ΔS1-Q387R and PNPase-ΔS1-E475G, share a similar structure to the crystal structure of dimeric PNPase-ΔS1-NHis.

We generated R_g-based dimensionless Kratky plots and revealed that both trimeric and dimeric PNPase exhibit a low degree of flexibility, with curve peaks at q^*R_g slightly greater than $\sqrt{3}$ (Figure 4B) (33). Furthermore, DAMMIF *ab initio* modeling (34) resulted in multiple envelopes for both forms of PNPase. Therefore, we modeled the structure of PNPase by the EOM, using the crystal structures of trimeric and dimeric PNPase and a modeled S1 domain as the rigid bodies (31). The experimental SAXS data fitted well with the calculated SAXS profiles from the selected ensembles of the trimeric and dimeric forms of PNPase (Figure 4C and D). The S1 domains in both trimeric and dimeric PNPase were flexible in that they could be fully extended in an open conformation or associated with the enzyme in a closed conformation. Trimeric PNPase-CHis had 55% of its ensembles in the open conformation and 45% in the closed conformation (Figure 4E). Interestingly, the S1 domains in the closed conformation of trimeric PNPase-CHis formed an S1 pore that was sufficiently wide to accommodate a small stem–loop RNA, suggesting that the S1 pore is likely the binding site for the stem–loop motif of imported structured RNAs (see 'Discussion' section).

The dimeric full-length PNPase proteins (PNPase-NHis, PNPase-Q387R and PNPase-E475G) also exhibited two major conformations, of which 33–50% were in an open conformation and 50–67% in a closed conformation (Figure 4F). In the closed conformation, the S1 domain was associated with the RNase PHII domain, making it less flexible and accessible for interacting with RNA. In the open conformation, the S1 domains were extended on opposing sides of the dimer, so they could not come together to form a pore to interact with stem–loop RNA. Therefore, we conclude that the S1 domains in the dimeric form of the disease-linked PNPase mutants are not fully accessible and so these mutants cannot bind the stem–loop motif of structured RNAs for import into mitochondria.

DISCUSSION

Here we show, for the first time, that disease-linked human PNPase mutants are assembled into a dimeric structure with a disrupted KH pore for ssRNA-binding. The KH domain is a typical nucleic acid-binding module that is found in single or usually multiple copies of proteins associated with transcriptional and translational regulation (35). All typical KH domains contain a GXXG motif located in a loop that forms a cleft with two α-helices for ssRNA or ssDNA binding. In the trimeric PNPase structure, the three KH domains form a KH pore, with the exposed GXXG motifs oriented inward toward the pore to facilitate interactions with ssRNA (23). In the crystal structure of *Caulobacter crescentus* PNPase, the three KH domains make nonequivalent interactions with a single RNA chain, suggesting a 'ratchet-type' model for pulling the RNA into the degradation channel (25). However, in the dimeric PNPase structure, the KH pore is disrupted and the GXXG motifs are far apart and less accessible for RNA binding. Our biochemical studies consistently show that dimeric PNPase has lower ssRNA binding and degrading activities compared to trimeric PNPase. Our findings explain why the disrupted KH pore of disease-linked PNPase mutants impairs ssRNA binding and degradation.

We also show here that the S1 domain of PNPase is involved in binding to the stem–loop motif of imported structured RNAs. The S1 domain is also a typical RNA-binding module, which was originally identified in the ribosomal protein S1 (36). A number of crystal and NMR structures of S1 domains in various ribonucleases involved in RNA turnover have been reported (including those of PNPase, RNase E and RNase R), revealing an oligonucleotide-binding fold (OB fold) with the RNA-binding surface located on one side of the β barrel (37–39). Here, we show that the S1 domains of trimeric human PNPase form a flexible extended open conformation, similar to the 'splayed' conformation identified in the crystal structure of *C. crescentus* PNPase that may facilitate capture of RNA substrates (25). The flexibility of S1 domain in PNPase has been observed in many structures, such as that the S1 domain was disordered in the RNA-bound *C. crescentus* PNPase (25) and that the S1 domain is shifted with different orientations in *C. crescentus* PNPase as compared to the one in *C. burnetii* PNPase (32). The S1 domain in human PNPase could also shift into a closed conformation to form an S1 pore, which is likely the binding site for the stem–loop motif of imported structured RNAs. Interestingly, a similar S1 pore, formed by three S1 proteins, was also observed in various crystal structures of RNA exosomes involved in RNA turnover (40,41). The S1 pore in exosomes has a pore size wide enough for binding of stem–loop RNAs as shown by the crystal structures of *Saccharomyces cerevisiae* exosome in complex with a loop RNA and a stem–loop RNA, respectively (42,43) (Figure 5). The S1 domains in the trimeric PNPase are likely more flexible to accomplish the function in capturing and binding stem–loop RNA for mitochondrial RNA import. We thus proposed a structural model of a trimeric PNPase bound with a stem–loop motif of RNase P RNA (Figure 5). The stem–loop RNA fits snuggly into this S1 pore in the trimeric PNPase, but it is too big to fit into the KH pore for further delivery into the RNase PH channel for degradation. Consequently, these structured RNAs are imported into mitochondria, but not degraded by human PNPase.

In contrast, the S1 domains in the closed form of dimeric PNPase are associated with the RNase PHII domains, making them inaccessible for RNA binding. Therefore, we conclude that the KH domains of trimeric PNPase are involved in ssRNA binding, whereas the flexible S1 domains are responsible for capture of RNA substrates in the open conformation and adopt a closed conformation (forming an S1 pore) upon binding of the stem–loop motif of structured RNA for mitochondrial RNA import (see Supplementary Movie S2). Any mutations that disrupt PNPase enzyme activity or its trimeric conformation inhibit its RNA degradation or import activities, leading to mitochondrial dysfunction and diseases. Investigations of the heterozygous variants Q254K/A510P (8) and G76D/R192* (10) will likely

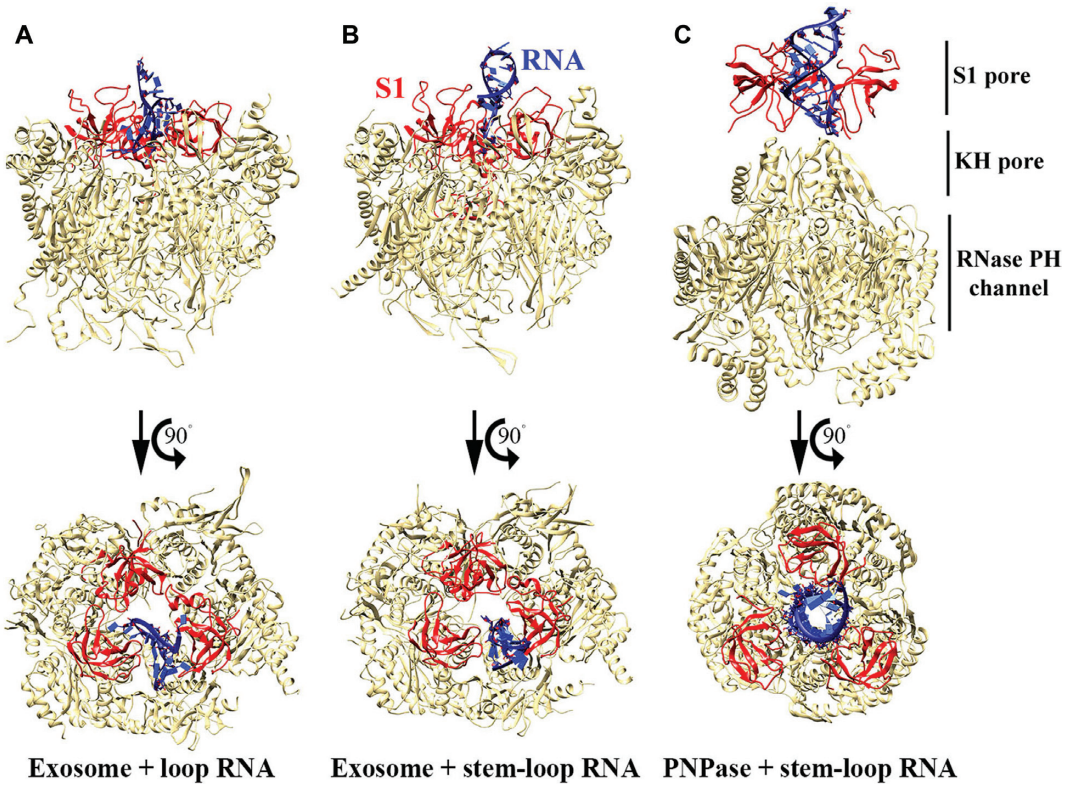

Figure 5. The S1 pore in RNA exosomes and PNPase. (**A**) Crystal structure of *Saccharomyces cerevisiae* nuclear exosome (PDB ID: 5K36) bound with a loop RNA in the S1 pore. (**B**) Crystal structure of *S. cerevisiae* cytoplasmic exosome (PDB ID: 5JEA) bound with a stem–loop RNA in the S1 pore. (**C**) Structural model of trimeric human PNPase bound with a stem–loop RNA in the S1 pore. The closed conformation of trimeric PNPase was generated by SAXS that was fitted with a stem–loop RNA of RNase P RNA (PDB ID: 1F6X). The S1 pore, KH pore and RNase PH degradation channel are labeled in the side view (top panel) of the PNPase structure. The S1 domains of RNA exosomes and PNPase are displayed in red and RNA are displayed in blue.

prove revealing, all of which are presumably defective in forming a functional trimeric PNPase.

DATA AVAILABILITY

Protein Data Bank (PDB, https://www.rcsb.org/): 5ZF6.

SUPPLEMENTARY DATA

Supplementary Data are available at NAR Online.

ACKNOWLEDGEMENTS

Portions of this research were carried out at the National Synchrotron Radiation Research Center, a national user facility supported by the Ministry of Science and Technology of Taiwan.

FUNDING

Academia Sinica; Ministry of Science and Technology, Taiwan, ROC. Funding for open access charge: Academia Sinica.
Conflict of interest statement. None declared.

REFERENCES

1. Wiedemann,N. and Pfanner,N. (2017) Mitochondrial machineries for protein import and assembly. *Annu. Rev. Biochem.*, **86**, 685–714.
2. Lithgow,T. and Schneider,A. (2010) Evolution of macromolecular import pathways in mitochondria, hydrogenosomes and mitosomes. *Phil. Trans. R. Soc. B*, **365**, 799–817.
3. Kim,K.M., Noh,J.H., Abdelmohsen,K. and Gorospe,M. (2017) Mitochondrial noncoding RNA transport. *BMB Rep.*, **50**, 164–174.
4. Wang,G., Shimada,E., Koehler,C.M. and Teitell,M.A. (2012) PNPASE and RNA trafficking into mitochondria. *Biochim. Biophys. Acta Gene Reg. Mech.*, **1819**, 998–1007.
5. Wang,G., Chen,H.W., Oktay,Y., Zhang,J., Allen,E.L., Smith,G.M., Fan,K.C., Hong,J.S., French,S.W., McCaffery,J.M. *et al.* (2010) PNPASE regulates RNA import into mitochondria. *Mol. Cell*, **142**, 456–467.
6. Ameln,S.V., Wang,G., Boulouiz,R., Rutherford,M.A., Smith,G.M., Li,Y., Pogoda,H.-M., Nürnberg,G., Stiller,B., Volk,A.E. *et al.* (2012) A mutation in *PNPT1*, encoding mitochondrial-RNA-import protein PNPase, causes hereditary hearing loss. *Am. J. Hum. Genet.*, **91**, 1–9.
7. Vedrenne,V., Gowher,A., De Lonlay,P., Nitschke,P., Serre,V., Boddaert,N., Altuzarra,C., Mager-Heckel,A.M., Chretien,F., Entelis,N. *et al.* (2012) Mutation in *PNPT1*, which encodes a polyribonucleotide nucleotidyltransferase, impairs RNA import into mitochondria and causes respiratory-chain deficiency. *Am. J. Hum. Genet.*, **91**, 912–918.
8. Alodaib,A., Sobreira,N., Gold,W.A., Riley,L.G., Van Bergen,N.J., Wilson,M.J., Bennetts,B., Thorburn,D.R., Boehm,C. and Christodoulou,J. (2017) Whole-exome sequencing identifies novel variants in *PNPT1* causing oxidative phosphorylation defects and severe multisystem disease. *Eur. J. Hum. Genet.*, **25**, 79–84.
9. Matilainen,S., Carroll,C.J., Richter,U., Euro,L., Pohjanpelto,M., Paetau,A., Isohanni,P. and Suomalainen,A. (2017) Defective mitochondrial RNA processing due to *PNPT1* variants causes Leigh syndrome. *Hum. Mol. Genet.*, **26**, 3352–3361.
10. Sato,R., Arai-Ichinoi,N., Kikuchi,A., Matsuhashi,T., Numata-Uematsu,Y., Uematsu,M., Fujii,Y., Murayama,K.,

Ohtake,A., Abe,T. *et al.* (2018) Novel biallelic mutations in the *PNPT1* gene encoding a mitochondrial-RNA-import protein PNPase cause delayed myelination. *Clin. Genet.*, **93**, 242–247.
11. Sarkar,D. and Fisher,P.B. (2006) Polynucleotide phosphorylase: An evolutionary conserved gene with an expanding repertoire of functions. *Pharmacol. Ther.*, **112**, 243–263.
12. Mohanty,B.K. and Kushner,S.R. (2000) Polynucleotide phosphorylase functions both as a 3′→ 5′ exonuclease and a poly(A) polymerase in *Escherichia coli*. *Proc. Natl. Acad. Sci. U.S.A.*, **97**, 11966–11971.
13. Andrade,J.M., Pobre,V., Silva,I.J., Domingues,S. and Arraiano,C.M. (2009) The role of 3′-5′ exoribonucleases in RNA degradation. *Prog. Mol. Biol. Transl. Sci.*, **85**, 187–229.
14. Deutscher,M.P. (2006) Degradation of RNA in bacteria: comparison of mRNA and stable RNA. *Nucleic Acids Res.*, **34**, 659–666.
15. Leszczyniecka,M., Kang,D.C., Sarkar,D., Su,Z.Z., Holmes,M., Valerie,K. and Fisher,P.B. (2002) Identification and cloning of human polynucleotide phosphorylase, hPNPase old-35, in the context of terminal differentiation and cellular senescence. *Proc. Natl. Acad. Sci. U.S.A.*, **99**, 16636–16641.
16. Sarkar,D., Leszczyniecka,M., Kang,D.C., Lebedeva,I.V., Valerie,K., Dhar,S., Pandita,T.K. and Fisher,P.B. (2003) Down-regulation of *myc* as a potential target for growth arrest induced by human polynucleotide phosphorylase (hPNPase(old-35)) in human melanoma cells. *J. Biol. Chem.*, **278**, 24542–24551.
17. Sarkar,D., Park,E.S. and Fisher,P.B. (2006) Defining the mechanism by which IFN-beta dowregulates *c-myc* expression in human melanoma cells: pivotal role for human polynucleotide phosphorylase (hPNPase(old-35)). *Cell Death Differ.*, **13**, 1541–1553.
18. Shepherd,D.L., Hathaway,Q.A., Pinti,M.V., Nichols,C.E., Durr,A.J., Sreekumar,S., Hughes,K.M., Stine,S.M., Martinez,I. and Hollander,J.M. (2017) Exploring the mitochondrial microRNA import pathway through polynucleotide phosphorylase (PNPase). *J. Mol. Cell. Cardiol.*, **110**, 15–25.
19. Chen,H.W., Rainey,R.N., Balatoni,C.E., Dawson,D.W., Troke,J.J., Wasiak,S., Hong,J.S., McBride,H.M., Koehler,C.M., Teitell,M.A. *et al.* (2006) Mammalian polynucleotide phosphorylase is an intermembrane space RNase that maintains mitochondrial homeostasis. *Mol. Cell. Biol.*, **26**, 8475–8487.
20. Rainey,R.N., Glavin,J.D., Chen,H.W., French,S.W., Teitell,M.A. and Koehler,C.M. (2006) A new function in translocation for the mitochondrial i-AAA protease Yme1: import of polynucleotide phosphorylase into the intermembrane space. *Mol. Cell. Biol.*, **26**, 8488–8497.
21. Wang,D.D.-H., Shu,Z., Lieser,S.A., Chen,P.-L. and Lee,W.-H. (2009) Human mitochondrial SUV3 and polynucleotide phosphorylase form a 330-kDa heteropentamer to cooperatively degrade double-stranded RNA with a 3-to-5 directionality. *J. Biol. Chem.*, **284**, 20812–20821.
22. Das,S.K., Bhutia,S.K., Sokhi,U.K., Dash,R., Azab,B., Sarkar,D. and Fisher,P.B. (2011) Human polynucleotide phosphorylase (hPNPaseold-35): an evolutionary conserved gene with an expanding repertoire of RNA degradation functions. *Oncogene*, **30**, 1733–1743.
23. Lin,C.L., Wang,Y.T., Yang,W.Z., Hsiao,Y.Y. and Yuan,H.S. (2012) Crystal structure of human polynucleotide phosphorylase: insights into its domain function in RNA binding and degradation. *Nucleic Acids Res.*, **40**, 4146–4157.
24. Shi,Z., Yang,W.Z., Lin-Chao,S., Chak,K.F. and Yuan,H.S. (2008) Crystal structure of *Escherichia coli* PNPase: central channel residues are involved in processive RNA degradation. *RNA*, **14**, 2361–2371.
25. Hardwick,S.W., Gubbey,T., Hug,I., Jenal,U. and Luisi,B.F. (2012) Crystal structure of *Caulobacter crescentus* polynucleotide phosphorylase reveals a mechanism of RNA substrate channelling and RNA degradosome assembly. *Open Biol.*, **2**, 120028.
26. Nurmohamed,S., Vaidialingam,B., Callaghan,A.J. and Luisi,B.F. (2009) Crystal structure of *Escherichia coli* polynucleotide phosphorylase core bound to RNase E, RNA and manganese: implications for catalytic mechanism and RNA degradosome assembly. *J. Mol. Biol.*, **389**, 17–33.
27. Portnoy,V., Palnizky,G., Yehudai-Resheff,S., Glaser,F. and Schuster,G. (2008) Analysis of the human polynucleotide phosphorylase (PNPase) reveals differences in RNA binding and response to phosphate compared to its bacterial and chloroplast counterparts. *RNA*, **14**, 297–309.
28. Wong,A.G., McBurney,K.L., Thompson,K.J., Stickney,L.M. and Mackie,G.A. (2013) S1 and KH domains of polynucleotide phosphorylase determine the efficiency of RNA binding and autoregulation. *J. Bacteriol.*, **195**, 2021–2031.
29. Siomi,H., Matunis,M.J., Michael,W.M. and Dreyfuss,G. (1993) The pre-mRNA binding K protein contains a novel evolutionarily conserved motif. *Nucleic Acids Res.*, **21**, 1193–1198.
30. Kopec,J. and Schneider,G. (2011) Comparison of fluorescence and light scattering based methods to assess formation and stability of protein-protein complexes. *J. Struct. Biol.*, **175**, 216–223.
31. Petoukhov,M.V., Franke,D., Shkumatov,A.V., Tria,G., Kikhney,A.G., Gajda,M., Gorba,C., Mertens,H.D., Konarev,P.V. and Svergun,D.I. (2012) New developments in the program package for small-angle scattering data analysis. *J. Appl. Cryst.*, **45**, 342–350.
32. Franklin,M.C., Cheung,J., Rudolph,M.J., Burshteyn,F., Cassidy,M., Gary,E., Hillerich,B., Yao,Z.K., Carlier,P.R., Totrov,M. *et al.* (2015) Structural genomics for drug design against the pathogen *Coxiella burnetii*. *Proteins*, **83**, 2124–2136.
33. Receveur-Brechot,V. and Durand,D. (2012) How random are intrinsically disordered proteins? A small angle scattering perspective. *Curr. Protein Pept. Sci.*, **13**, 55–75.
34. Franke,D. and Svergun,D.I. (2009) DAMMIF, a program for rapid ab-initio shape determination in small-angle scattering. *J. Appl. Cryst.*, **42**, 342–346.
35. Valverde,R., Edwards,L. and Regan,L. (2008) Structure and function of KH domains. *FEBS J.*, **275**, 2712–2726.
36. Subramanian,A.R. (1983) Structure and functions of ribosomal protein S1. *Prog. Nucleic Acid Res. Mol. Biol.*, **28**, 101–142.
37. Bycroft,M., Hubbard,T.J.P., Proctor,M., Freund,S.M.V. and Murzin,A.G. (1997) The solution structure of the S1 RNA binding domain: A member of an ancient nucleic acid–binding fold. *Cell*, **88**, 235–242.
38. Schubert,M., Edge,R.E., Lario,P., Cook,M.A., Strynadka,N.C.J., Mackie,G.A. and McIntosh,L.P. (2004) Structural characterization of the RNase E S1 domain and identification of its oligonucleotide-binding and dimerization Interfaces. *J. Mol. Biol.*, **341**, 37–54.
39. Chu,L.-Y., T.-J.,H., Golzarroshan,B., Chen,Y.-P., Agrawal,S. and Yuan,H.S. (2017) Structural insights into RNase R in RNA unwinding and degradation. *Nucleic Acids Res.*, **45**, 12015–12024.
40. Buttner,K., Wenig,K. and Hopfner,K.P. (2005) Structural framework for the mechanism of archaeal exosomes in RNA processing. *Mol. Cell*, **20**, 461–471.
41. Liu,Q.S., Greimann,J.C. and Lima,C.D. (2007) Reconstitution, activities, and structure of the eukaryotic RNA exosome. *Cell*, **131**, 188–189.
42. Makino,D.L., Baumgartner,M. and Conti,E. (2013) Crystal structure of an RNA-bound 11-subunit eukaryotic exosome complex. *Nature*, **495**, 70–75.
43. Zinder,J.C., Wasmuth,E.V. and Lima,C.D. (2016) Nuclear RNA exosome at 3.1 angstrom reveals substrate specificities, RNA paths, and allosteric Inhibition of Rrp44/Dis3. *Mol. Cell*, **64**, 734–745.